Ultra-selective *p*-xylene production through cycloaddition and dehydration of 2,5-dimethylfuran and ethylene over tin phosphate

Xinqiang Feng[a], Ziheng Cui[a], Kaiyue Ji[a], Chun Shen[a,b], Tianwei Tan[a,*]

[a] *Beijing Key Laboratory of Bioprocess, National Energy R&D Center for Biorefinery, Beijing University of Chemical Technology, No. 15 of North Three-Ring East Road, Chaoyang District, Beijing 100029, PR China*
[b] *The State Key Laboratory of Chemical Engineering, Department of Chemical Engineering, Tsinghua University, Beijing 100084, PR China*

ARTICLE INFO

ABSTRACT

A series of SnPO catalysts was systematically prepared and characterized in detail to provide an insight into the structure-activity relationship for PX production from 2,5-dimethylfuran (DMF) and ethylene. SnPO possessing tetrahedrally coordinated Sn(IV) as the active sites exhibited an ultra-high PX yield of 93%. The outstanding catalytic performance of SnPO could be ascribed to two aspects: a controllable adjustment in acid sites (tetrahedrally coordinated Sn(IV) or P−OH) by altering the molar ratio of P/Sn, which leads to enhancement in the main reaction and inhibition for the side reactions; the improved mass transfer efficiency and high tolerance to deactivation caused by carbon deposition because of the mesoporous structure. The DFT calculation revealed that tetrahedrally coordinated Sn(IV) was more efficient than P−OH groups for PX production. The ultra-high activity and stability of SnPO should allow significant progress in the efficient production of bio-based PX in the near future.

1. Introduction

p-Xylene (PX), one of the important bulk organic chemicals, is a precursor for the production of polyethylene terephthalate (PET). PET is a widely used polymer mainly to produce fibers, plastic containers and packaging films [1–4]. The consumption of PET is about 100 million tons one year and is still growing at a rate of 4% per year, which makes PX one of the most demanded commodity chemicals because of its huge market demand [5,6].

Conventionally, PX is refined from petroleum-derived naphtha. To reduce greenhouse gas emission and enhance the utilization of renewable feedstock, the production of bio-based PX has attained significant attention [5,7,8]. In recent years, a promising route via 2,5-dimethylfuran (DMF) has been explored for the production of renewable PX [9,10]. The first step of this route is the preparation of 5-hydroxymethylfurfural (HMF) from dehydration of hexoses (glucose or fructose). The first commercial-scale production of HMF (20 T per year) from biomass has been achieved by the AVA Biochem company in Switzerland in 2014 [11]. Subsequently, HMF is further hydrodeoxygenated to DMF by catalytic hydrogenation. It has been reported that the yield of DMF from HMF can exceed 98% over both noble metal catalysts(i.e., Pt−Co bimetallic catalysts) [12] and non-noble metal catalysts (i.e., Cu−Co bimetallic catalysts) [13,14]. Finally, DMF reacts with ethylene to prepare PX over a solid acid catalyst.

The conversion process of DMF and ethylene to form PX can be divided into two steps as shown in Fig. 1. The first step is the Diels–Alder reaction of DMF and ethylene to form the cycloadduct intermediate (with an activation barrier of 24.7 kcal/mol), which is thermally feasible as reported by Vlachos, et al [15]. It can be catalyzed by Lewis acid, while Brønsted acid exhibits no catalytic reactivity [15]. The next step is the subsequent dehydration of the cycloadduct to produce PX (with an activation barrier of 58.0 kcal/mol) [15], which cannot proceed uncatalyzed. The introduction of Lewis or Brønsted acids can effectively initiate the occurrence of the dehydration reaction. Normally, Brønsted acid exhibits a lower activation energy than Lewis acid [16]. The main side reaction is the hydrolysis of DMF to produce 2,5-hexanedione (HDO). Furthermore, the hydrolysis by-product HDO condensates intramolecularly to produce 3-methyl-2-cyclopentenone (MCP) and HDO condensates intermolecularly to form the insoluble surface polymerized products via aldol reactions in the acid environment [9,17]. In addition, there is a small amount of over alkylated products (OAP), 1-methyl-4-propylbenzene and 1,3-dimethyl-2-ethylbenzene, produced in the reaction, resulting from the excessive alkylation of PX with ethylene. The cycloadduct intermediate undergoes isomerization to form 3,6-dimethyl-2-cyclohexenone (DMCHO) [18].

* Corresponding authors at: Beijing Key Laboratory of Bioprocess, National Energy R&D Center for Biorefinery, Beijing University of Chemical Technology, No. 15 of North Three-Ring East Road, Chaoyang District, Beijing 100029, PR China.
E-mail addresses: shenchun@mail.buct.edu.cn (C. Shen), twtan@mail.buct.edu.cn (T. Tan).
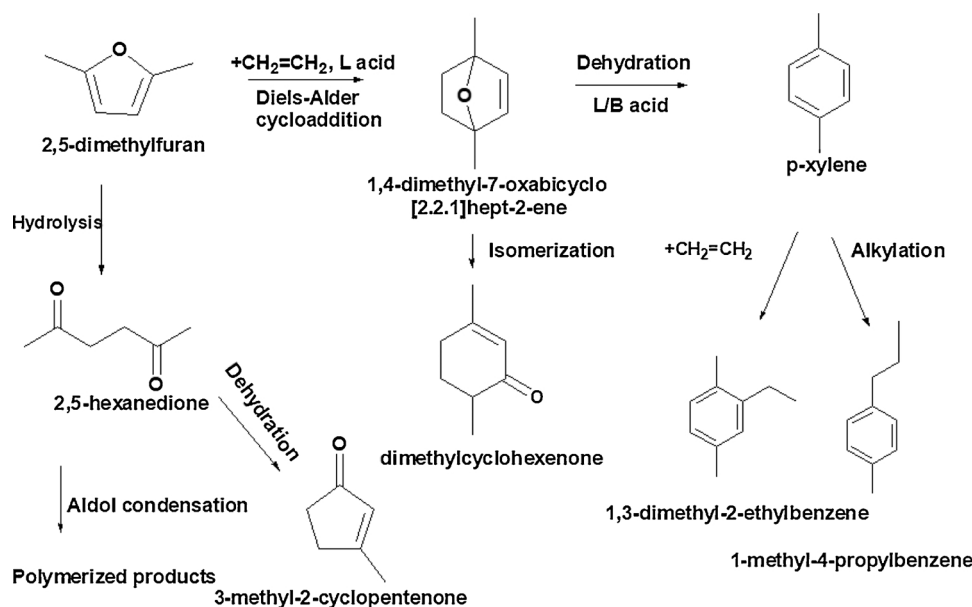
Fig. 1. Schematic diagram of the reaction of DMF and ethylene to produce P X .

Over the last few years, intensive research has been performed on several kinds of solid acid catalysts for highly selective production of PX . Zeolites such as H--Y, H-Beta, Sn-Beta, and P-Beta are reported to be the efficient catalysts for PX production [10,17,19–22]. H--Y and H-Beta zeolite can achieve a PX selectivity of 75% and 80%, respectively. However, the inherent microporous structures of the zeolites such as H-Beta and H--Y have an adverse effect on the mass transfer and catalytic activity. The polymerized products are apt to be trapped in the small pores of zeolite catalysts, leading to coke formation and catalytic de-activation. Subsequent research focused on improving the mass transfer performance of zeolite-based catalysts by introducing mesopores as reported by Kim et al [20,23]. Mesoporous solid acid such as WO_3/ZrO_2 and heteropolyacid supported catalysts were also found to be highly selective for PX production (about 80–85% PX selectivity) [24,25]. Therefore, from the view of the structural properties, mesoporous acid catalysts are more suitable for PX production.

Sn-Beta and Zr-Beta, which possess metal sites in unsaturated co-ordination as Lewis acid sites, can achieve a high PX selectivity of 80% and 90%, respectively, as reported by Fan, et al [17]. Since Lewis acid sites have a slower production rate of HDO and are not efficient for catalyzing condensation reactions of HDO. Lewis acidic materials ap-pear to be better suited for the highly selective production of PX than Brønsted acidic materials as proposed by Gorte, et al [16]. To date, P-Beta is found to achieve the highest PX selectivity of 97% as reported by Fan, et al [21]. Unlike other Brønsted acidic catalysts, P-Beta which possesses P−OH group exhibits outstanding catalytic performance be-cause of its low catalytic ability for side reactions. While, the stability of P-Beta needs to be further improved [21,26].

Considering the issues mentioned above, we specially designed tin phosphate (SnPO) which has tetrahedrally coordinated Sn(IV) and P−OH as the catalyst for highly selective production of PX . As a me-soporous solid acid catalyst, SnPO has favourable catalytic character-istics such as controllable acidity, water tolerant Brønsted and Lewis acid sites, mesoporous structure, and high thermal stability [27–29]. It has been widely used in the field of heterogeneous acid-catalyzed re-actions, such as dehydration and esterification reactions [30–32]. To the best of our knowledge, the application of SnPO towards PX pro-duction from DMF has not been reported yet. There may be three po-tential advantages by choosing SnPO as the catalyst. (1) The meso-porous structure is apt to facilitate the mass transfer efficiency and feature a strong ability to resist carbon deposition, improving the cat-alyst stability. (2) The active sites, namely tetrahedrally coordinated Sn

(IV) and P−OH group, tend to achieve a high selectivity for PX pro-duction. (3) The Lewis and Brønsted acidity could be controllably ad-justed by varying the quantity ratio of the tetrahedrally coordinated Sn (IV) and P−OH group, giving deeper insight into their respective con-tribution to the catalytic performance.

Herein, we explored the physicochemical properties of SnPO cata-lysts as well as their catalytic performances for PX production from DMF and ethylene. In addition, their catalytic performances were compared with zeolite-based catalysts (H-Beta, Sn-Beta, and P-Beta), which were previously reported as particularly effective catalysts for PX production. Reaction kinetics on SnPO catalysts and zeolite-based cat-alysts revealed the difference in the activation energies and catalytic activity. Additionally, density functional theory (DFT) calculations were performed to better elucidate the role of the active sites on SnPO catalysts in the catalytic activity. Besides, the stability test and re-generation performance were investigated systematically.

2. Experimental section

2.1. Materials and chemicals

Triblock copolymer P123 ($EO_{20}PO_{70}EO_{20}$, average Mn = 5800) was obtained from Aldrich. *N*-heptane, *n*-decane, and H_3PO_4 (85 wt%) were all analytically pure and purchased from Beijing Chemical Plant. Analytical grade $SnCl_4·5H_2O$ was purchased from Sigma. Analytical grade DMF was purchased from Xiya Chemical Plant in Shandong, China. Tetrahydrofuran (HPLC grade) was purchased from Fisher Chemical Corporation. Ethylene (99.5%) and nitrogen (99.999%) was purchased from Haipu Gas Corporation in Beijing, China. All chemicals were used as received without further treatment.

2.2. Material synthesis

The synthesis of SnPO-x (x represents the molar ratio of P/Sn in the preparation course) with different P/Sn followed the procedure re-ported by Saha, et al. [33] In a typical synthesis, P123 (4.0 g) and phosphoric acid (4.6 g, 40 mmol) were added to H_2O (60 g) at 30 °C. It was stirred for 3 h until a clear solution was obtained. $SnCl_4·5H_2O$ (14.0 g, 40 mmol) was dissolved in H_2O (20 g) and then it was added to the above H_3PO_4 solution dropwise. The mixture was stirred for another 3 h. Subsequently, it was transferred into a Teflon-lined stainless steel autoclave and kept at 100 °C for 72 h. The resulted white precipitate

was separated by filtration and washed by water and ethanol for several times. Finally, it was dried at 80 °C and calcined at 550 °C for 6 h to obtain SnPO-1.00. SnPO with other molar ratios of P/Sn was prepared following the same procedure but by varying the molar ratio of P/Sn. And SnPO prepared in the absence of P123 (denoted as sSnPO) was prepared following the same procedure but without P123 added.

H-Beta (Si/Al = 12.5) was purchased from Nankai University Catalyst Co., Ltd. The preparation methods of Sn-Beta and P-Beta were described in the Supplementary data [21,34].

2.3. Characterization

The surface morphology of catalysts was analyzed by JEOL JSM-7800 F schottky field emission scanning electron microscope (SEM) and JEOL JEM-2010 high-resolution transmission electron microscope (HRTEM) at an accelerating voltage of 120 kV.

Nitrogen adsorption/desorption isotherms were measured on a Micromeritics ASAP 2020 HD88 surface area and porosity analyzer. The catalysts were degassed at 350 °C for 7 h before measurements. The Brunauer-Emmett-Teller (BET) procedure was used to calculate the surface area. The pore size distribution was calculated by using the Density Functional Theory (DFT) method. The pore volume was calculated at a relative pressure of approximately 0.99.

Powder wide-angle and small-angle X-ray diffraction (XRD) patterns were recorded on a RINT2000 vertical goniometer with Cu Kα radiation (λ = 0.154 nm), operated at 40 kV and 50 mA.

The total acidity of catalysts was determined by temperature-programmed desorption of NH_3 (NH_3-TPD) in a Micromeritics AutoChem II 2920 chemisorption analyzer. The sample was pretreated at 400 °C for 1 h in He. Then NH_3 (5 vol% NH_3 in He) was introduced for 0.5 h at 100 °C. After that, the sample was treated with He for 0.5 h to remove the physically adsorbed NH_3 and the TCD signal was recorded from 100 °C to 800 °C at a heating ramp of 10 °C/min.

Fourier transform infrared (FT-IR) spectra of the SnPO were recorded on a Nicolet 6700 IR spectrometer (Thermo corporation, USA) using the KBr disc method. The pyridine adsorption FTIR (Py-FTIR) spectra were performed on a Bruker Tensor 27 FT-IR spectrometer. The sample was first pretreated under vacuum at 400 °C for 1 h. Then it was cooled to 100 °C and pyridine was introduced for 0.5 h followed by recording the background spectra. The pyridine adsorption spectra were recorded at 150 °C and 350 °C, respectively. The ratio of Lewis to Brønsted acid sites was calculated by using the peak areas at 1450 cm⁻¹ and 1540 cm⁻¹, respectively.

Diffuse-reflectance ultraviolet-visible (DR UV-vis) spectra were recorded on a UV-3600 spectrophotometer (Shimadzu Corporation, Japan) to determine the coordination state of Sn species.

The element contents of Sn and P in the solid acid catalysts were measured by inductively coupled plasma optical emission spectroscopy (ICP-OES) analysis on an iCAP 6000 Series spectrometer (Thermo Scientific, USA). The samples were dissolved thoroughly in aqua regia under microwave irradiation before the measurements.

X-ray photoelectron spectroscopy (XPS) was performed on ESCALAB 250 (ThermoFisher Scientific, USA) using a monochromatic Al K (alpha) source (150 W) to examine the valence states of individual elements in the catalyst and the surface atomic composition.

Solid state ^{31}P-NMR spectra and ^{13}C CP-MAS NMR were recorded on a Bruker AV300 spectrometer. The operating frequency was 202.5 MHz for ^{31}P. Samples packed into 4 mm zirconia rotors were spun at 12 kHz. ^{31}P chemical shifts were externally referenced to 85% H_3PO_4. ^{13}C CP-MAS NMR was performed with 75.46 MHz spectrometer frequency and 4.17 kHz spectral width. Tetramethylsilane was used as chemical shift reference.

Thermogravimetric analysis (TGA) was performed on a Discovery TGA 55 with a heating rate of 10 °C/min⁻¹ in air.

The adsorption characteristics of reactants on catalysts were determined by temperature-programmed desorption analyzer with a mass

spectrometer (TPD-MS) on a Micromeritics Autochem 2910 chemisorption analyzer and Pfeiffer Omnistar. Before performing the adsorption experiment, 50 mg sample was pretreated at 300 °C for 1 h. Then sample was cooled to room temperature and saturated with DMF by exposure to the vapors for 0.5 h. After adsorbing DMF, ethylene was introduced for 0.5 h. The sample was treated with He for 0.5 h to remove the physically adsorbed DMF or ethylene and the MS signals were recorded from 30 °C to 350 °C at a heating ramp of 10 °C/min.

2.4. Catalyst activity

The details of the activity tests are available in the Supplementary data. DMF conversion (X), product selectivity (S_i) and yield (Y_i) were calculated according to the following Eqs. (1)–(3), respectively.

$$X(\%) = 100 \times \frac{C_{DMF,t_0} - C_{DMF,t}}{C_{DMF,t_0}} \tag{1}$$

$$S_i(\%) = 100 \times \frac{C_{i,t}}{C_{DMF,t_0} - C_{DMF,t}} \tag{2}$$

$$Y_i(\%) = 100 \times \frac{C_i}{C_{DMF,t_0}} \tag{3}$$

where C_{DMF,t_0} is the concentration of DMF before the reaction starts, $C_{DMF,t}$ is the concentration of DMF at a reaction time of t, and $C_{i,t}$ is the concentration of product i at a reaction time t.

The turnover frequency (TOF) for the conversion of DMF on each catalyst was calculated by normalizing the conversion rate of DMF by the number of acid sites as shown in Eqs (4). Similarly, the productivity of each product was calculated by normalizing the production rate of the corresponding product by the number of acid sites as shown in Eqs (5).

$$TOF \, (mol_{DMF} \cdot mol_{acid\,sites}^{-1} \cdot h^{-1}) = \frac{n_{converted\,DMF}}{n_{acid\,sites} \times t} \tag{4}$$

$$productivity \, (mol_i \cdot mol_{acid\,sites}^{-1} \cdot h^{-1}) = \frac{n_i}{n_{acid\,sites} \times t} \tag{5}$$

where $n_{converted\,DMF}$ is the moles of the converted DMF, n_i is the moles of the produced i, $n_{acid\,sites}$ is the moles of acid sites, and t is the reaction time.

2.5. DFT calculation method

In this work, geometry optimizations and transition states search were calculated by the Gaussian 09 software package with the B3LYP functional [35]. The adsorbates, the hydrogen atoms, the oxygen atoms and the phosphorus atoms were modeled with the 6-311 + G (d,p) basis set, while the tin atom was modeled with the effective core potential basis set LANL2DZ. The frequency of structures was also calculated at same level to ensure that the stable structures had no imaginary frequency, and only one imaginary frequency for the transition state.

3. Results and discussion

3.1. Controllable synthesis of SnPO catalysts

3.1.1. Physicochemical structure and morphology

The small-angle and wide-angle XRD patterns of SnPO were shown in Fig. S1(a) and (b), respectively. There were no distinct characteristic peaks for SnPO catalysts with the P/Sn of 1.00 and 1.25, indicating they were amorphous materials [30,31,33]. When the P/Sn was higher than 1.50, the diffraction peaks around 21° and 36° appeared, which could be indexed to those of $Sn(HPO_4)_2 \cdot H_2O$ (JCPDS, no. 31-1397) as shown in Fig. S1(b). However, the missing of the characteristic peak of $Sn(HPO_4)_2 \cdot H_2O$ at 25° and the broad diffraction peaks indicated that the crystallinity of SnPO catalysts was very low, suggesting that SnPO-1.50, 1.75 and 2.00 were mainly in amorphous form [36].
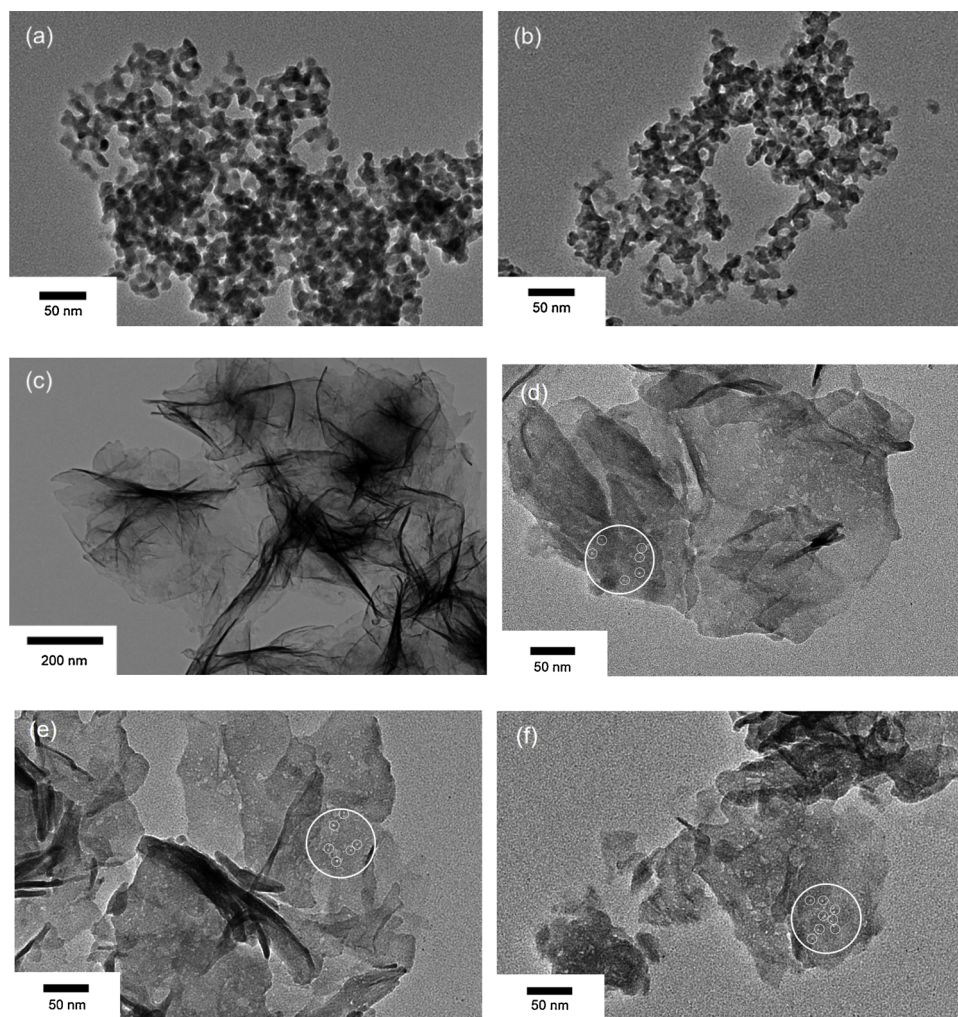
Fig. 2. TEM images of (a) SnPO-1.00, (b) SnPO-1.25, (c) and (d) SnPO-1.50, (e) SnPO-1.75, (f) SnPO-2.00.

SEM (Fig. S2) and TEM images (Fig. 2) show that SnPO-1.00 and SnPO-1.25 are composed of spherical nanoparticles. When the molar ratio of P/Sn was above 1.50, the superstructures of SnPO however became planar layered structure as shown in Fig. 2(c–f). It could also be clearly observed that mesopores were distributed on the surface of the nanosheets in Fig. 2(d–f). The layered structure and the presence of pores could promote mass transfer between catalyst and reactants, thus leading to improve the catalytic activity [37–39].

As shown in Fig. S3(a), the N_2 adsorption/desorption isotherms of SnPO with different molar ratio of P/Sn were all type IV isotherms with a H4 hysteresis loop in the high relative pressure region, as seen in the accumulation of nanoparticles or nanosheets in accordance with the SEM and TEM results [37]. The pore distributions of SnPO (Fig. S3(b) and (c)) indicated that all of the SnPO materials contained abundant mesopores (10–50 nm) and macropores (50–100 nm) resulting from the accumulation of nanoparticles or nanosheets. However, for SnPO-1.50, 1.75, and 2.00, a peak around 3.4 nm appeared (Fig. S3c), which might be resulted from the template P123. And the pores around 3.4 nm could be clearly observed in the TEM images (Fig. (3d–f)). Other BET results were summarized in Table S1.

3.1.2. Acid properties

The total acidity of SnPO was quantified by NH$_3$-TPD measurement. The NH$_3$ desorption profiles of SnPO were shown in Fig. S4(a). All of these materials showed only one NH$_3$ desorption peak at around 205 °C, indicating the presence of weak-to-medium acid sites [40,41]. The

Lewis and Brønsted acid properties were investigated by py-FTIR spectra as shown in Fig. S4(b). The adsorption peaks at 1450 and 1540 cm^{-1} were assigned to the adsorbed pyridine on Lewis and Brønsted acid sites, respectively. It could be clearly observed that the main acid types changed from Brønsted acid to Lewis acid with the increase of the molar ratio of P/Sn, and the detailed reason was discussed in the following part. The density of Brønsted and Lewis acid sites were calculated based on the NH$_3$-TPD and py-FTIR results as summarized in Table 1.

3.1.3. The analysis of active sites on SnPO catalysts

DR UV–vis spectroscopy was used to investigate the coordination states of Sn species. As shown in Fig. 3(a), SnO$_2$ which had octahedrally coordinated tin species, showed a broad absorption peak between 220

Table 1

Acid properties of SnPO with different molar ratio of P/Sn.

P/Sn	Total acid site density[a] (μmol/g)	Lewis acid site density (μmol/g)	Brønsted acid site density (μmol/g)	The ratio of L/B[b]
1.00	253	46	207	0.22
1.25	273	51	222	0.23
1.50	300	196	104	1.88
1.75	330	297	33	9.09
2.00	408	381	27	14.29

[a] Determined from NH$_3$-TPD measurements.
[b] Determined from py-FTIR measurements.
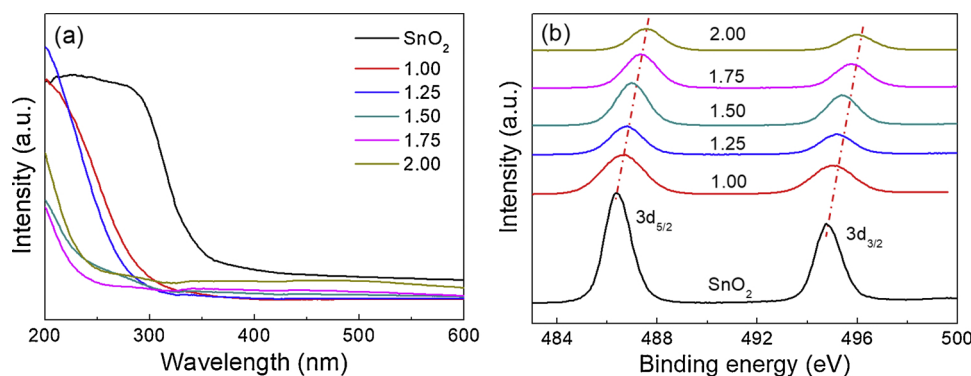
Fig. 3. (a) UV–vis DRS spectra of SnO_2 and SnPO catalysts with different molar ratio of P/Sn; (b) High resolution XPS spectra of the Sn3d on SnPO with different molar ratio of P/Sn and SnO_2.

and 280 nm. For SnPO catalysts, an intense band around 200 nm appeared, demonstrating that no bulk SnO_2 phase was formed and the tin species existed in tetrahedral coordination [42,43]. The tetrahedrally coordinated Sn(IV) in SnPO catalysts was often assumed to be the catalytically active sites [30,32]. The FTIR spectra of SnPO catalysts with different molar ratio of P/Sn (Fig. S5) showed a sharp band centered at $1130\ cm^{-1}$, assigned to the asymmetric Sn−O−P stretching vibration, proving the formation of Sn−O−P bonds [28,30,32,33]. XPS measurements (Fig. 3(b) and Fig. S6) were carried out to study the surface atomic compositions and oxidation states of the individual elements present in SnPO catalysts. The spectra of Sn 3d as shown in Fig. 3(b) consisted of two binding energy peaks at approximately 486.4 eV and 494.8 eV for SnO_2, corresponding to $3d_{5/2}$ and $3d_{3/2}$, respectively. This was a characteristic of tetravalent tin Sn(IV). For SnPO catalysts, the binding energy peaks of Sn shifted to higher values indicating the enhanced Lewis acidity than SnO_2 [32,44,45]. Furthermore, with the increase of molar ratios of P/Sn, a significant upward shift in the Sn3d binding energies was observed (Table S2), indicating an increased polarization of the Sn−O bonds and formation of more SnOO bonds and formation of more Sn−O−P bonds [44]. Therefore, the Lewis acidity increased with the increase of molar ratios of P/Sn. Besides, the atomic compositions on the surface and in the whole material were listed in Table S2. It was found that the molar ratios of P/Sn on the surface were higher than in the bulk, probably due to a preferential phosphorylation modification on the surface than inside the material.–

Solid state ^{31}P-NMR spectroscopy was used to explore the chemical interaction of the P atoms in SnPO catalysts. As shown in Fig. 4, four different resonance peaks appeared at -14, -20, -28 and -35 ppm. The resonance peak at -14 and -20 ppm could be assigned to (Sn−O)–PO $(OH)_2$ and $(Sn−O)_2$–PO(OH), respectively [21,26,31]. These two kinds of coordination states could supply terminal PO−H, which contributed to the Brønsted acidity. The resonance peak at -28 ppm could be attributed to $(Sn−O)_3$–PO. The resonance peak at -35 ppm implies the existence of polyphosphates, P−O−P as the result of the condensation of phosphate species. Overall, with the increased molar ratio of P/Sn, the chemical shift of P moved to a more negative value, indicating both an increase in the number of P−O−Sn bonds and an increase in the chain length of the phosphorus atoms [30,31]. Furthermore, the NMR spectra were deconvoluted using Origin software and the resonance bands were fitted with Lorentzian line shapes. The area ratio of the four resonance peaks represented the relative amounts of the different phosphate species as listed in Table 2. For SnPO-1.00 and SnPO-1.25, about 70% of P atoms possessed terminal P−OH, which made them mainly exhibit Brønsted acidity as shown in Table 1. With the increase of molar ratio of P/Sn, the amount of terminal P−OH kept decreasing, together with a decreasing Brønsted acidity. SnPO with a molar ratio of P/Sn above 1.50 mainly exhibited Lewis acidity. For SnPO-1.75, the ratio of L/B dramatically increased up to 9.09, probably due to a preferential phosphorylation modification on the surface over the inside of the

material (as observed in Table S2) leading to a dramatic decrease of PO−H on the surface.

Therefore, the Lewis acid derived from the tetrahedrally coordinated Sn(IV) and Brønsted acid derived from P−OH group. With the increased molar ratio of P/Sn, the amount of terminal P−OH kept decreasing, which led to a decreasing Brønsted acidity and an increasing ratio of Lewis to Brønsted acidity. It was easy and controllable to adjust the type of the acid sites by altering the molar ratio of P/Sn.

3.2. Catalytic evaluation of SnPO and structure-property relationship study

As expected, the SnPO catalysts did exhibit a satisfactory catalytic performance for PX production from DMF and ethylene. As listed in Table 3, SnPO-1.50 and SnPO-1.75 achieved a high PX selectivity of 90.4% (93.8% DMF conversion) and 92.1% (87.9% DMF conversion), respectively. Typically, a high PX selectivity of 93.3% with a conversion of 99.7% was observed on SnPO-1.75 after 18 h of reaction. Besides, it is worthwhile mentioning that the catalytic activity of SnPO catalysts varied with the P/Sn ratio: higher P/Sn ratio had a positive effect on the PX yield. With one exception, SnPO-2.00 exhibited a lower PX yield than SnPO-1.75. PX yield was related with both the activity of acid sites and the pore structure of the catalyst [19,23,24]. Given that SnPO-2.00 had similar acid property with SnPO-1.75 as shown in Fig. S4, the reduced PX yield was probably due to the decreased surface area (Table S1) and poor mass transfer [37,46]. In addition, higher P/Sn ratio also contributed to higher PX selectivity via inhibiting the production of hydrolysis-derived by-products (HDO and MCP). SnPO prepared in the absence of P123 (denoted as sSnPO) exhibited a smaller surface area and pore volume than SnPO prepared in the presence of P123 as shown in Fig. S7 and Table S3. Lower DMF conversions and PX yields (Table S4) were observed on sSnPO.

We also investigated the difference in product selectivity over zeolite-based catalysts. The XRD patterns of the zeolite-based catalysts were depicted in Fig. S8, and their acid properties were shown in Fig. S9 and Table S5. All of H-Beta, Sn-Beta, and P-Beta exhibited a lower selectivity ($< 80\%$) than SnPO-1.50 and SnPO-1.75 as listed in Table 3.

In order to take a deeper insight into the structure-activity relationship, kinetic analysis was carried out to reveal the difference in catalytic activity of SnPO and zeolite-based catalysts. To eliminate mass transport limitations, the effect of stirring speed on the PX production rate was studied. It was found that the maximum production rate of PX was achieved when the stirring speed exceeded 900 rpm as shown in Fig. S10. Therefore, the reactions were carried out in a batch reactor with a stirring speed of 1000 rpm.

TOF values for the conversion of DMF on each catalyst were calculated by normalizing the conversion rate by the number of total acid sites, which were determined by NH_3-TPD results. In addition, the productivity of each product was calculated by normalizing the production rate by the number of total acid sites. In the reaction of DMF
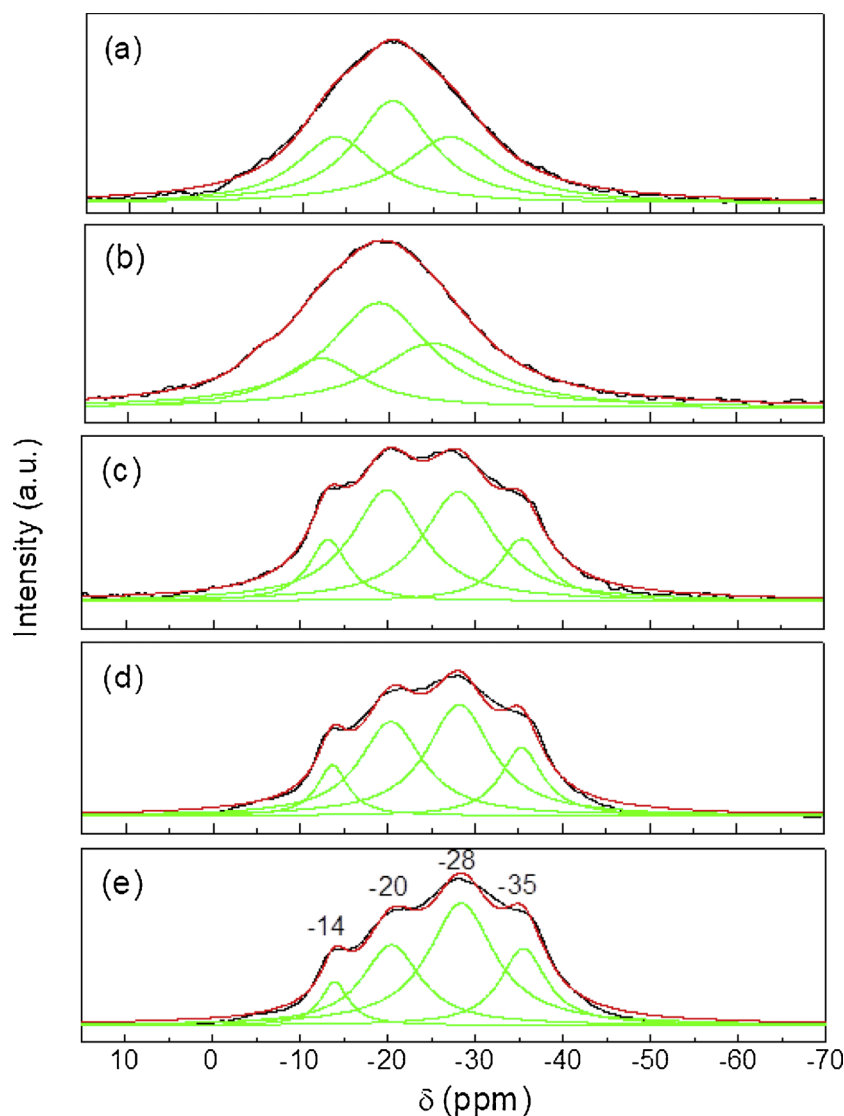
Fig. 4. ^{31}P solid state NMR spectra of (a) SnPO-1.00, (b) SnPO-1.25, (c) SnPO-1.50, (d) SnPO-1.75, and (e) SnPO-2.00.

and ethylene to produce PX, TOF and productivity of each product were shown in Fig. 5 and Fig. S11 (with a DMF conversion < 10% to ensure that the production rate was not limited by the reactant concentration as described in Fig. S12). SnPO-1.50 and SnPO-1.75 mainly possessing tetrahedrally coordinated Sn(IV) as the active sites exhibited significantly higher TOF values than SnPO-1.00 and SnPO-1.25 mainly possessing PO−H group as the active sites, suggesting that tetrahedrally coordinated Sn(IV) was more effective for DMF conversion during PX production than the acid sites PO−H in SnPO catalysts. Similar trend

was also observed for Beta catalysts, confirming the superior activity of tetrahedrally coordinated Sn(IV). In addition, the SnPO catalysts all exhibited a higher PX productivity than H-Beta, implying SnPO catalysts were more effective for PX production. Typically, SnPO-1.50 and SnPO-1.75 exhibited PX productivity of 155 $mol_{PX} \cdot mol_{acid\ sites}^{-1} h^{-1}$ and 173 $mol_{PX} \cdot mol_{acid\ sites}^{-1} h^{-1}$, respectively, which were nearly 1.5 times higher than H-Beta (108 $mol_{PX} \cdot mol_{acid\ sites}^{-1} h^{-1}$). They also demonstrated much lower activity for the main side reaction, namely hydrolysis of DMF, giving a lower productivity of 13 $mol_{HDO\ and\ MCP}$

Table 2
The relative amounts of the different phosphate species in SnPO with different molar ratio of P/Sn from solid state ^{31}P-NMR spectroscopy.

| Chemical shift (ppm)	−14	−20	−28	−35
Coordination group	HO, OH; P(=O), OSn	HO, OSn; P(=O), OSn	SnO, OSn; P(=O), OSn	PO, OP; P(=O), OSn
Catalyst	Relative amount (%)			
SnPO-1.00	27.5	42.9	29.6	negligible
SnPO-1.25	19.2	48.2	32.6	negligible
SnPO-1.50	11.4	37.3	37.4	13.9
SnPO-1.75	8.9	33.6	41.1	16.4
SnPO-2.00	7.0	26.7	46.1	20.2

Table 3
Catalytic results of SnPO with different molar ratio of P/Sn and zeolite-based catalysts for the reaction of DMF and ethylene to produce P X . (Reaction condition: DMF concentration, 1.04 M; initial ethylene pressure, 2.0 MPa; acid site concentration: 4.0 mM; reaction temperature, 250 °C; reaction duration: 6 h.).

Catalyst	DMF conversion (%)	PX yield (%)	Selectivity (%)					
			PX	OAP	DMCHO	HDO	MCP	Unknown
H-Beta	61.6	36.1	58.6	1.4	4.0	5.6	5.3	25.1
Sn-Beta	65.6	46.4	70.8	0.9	2.5	2.6	6.9	16.3
P-Beta	76.7	66.1	77.0	0.1	0.7	4.8	2.4	15.0
SnPO-1.00	78.5	48.9	72.5	1.0	1.2	7.7	1.5	16.1
SnPO-1.25	81.5	49.7	71.7	1.0	1.1	7.9	1.0	17.3
SnPO-1.50	93.8	84.8	90.4	0.9	0.4	3.5	1.0	3.8
SnPO-1.75	87.9	81.0	92.1	0.8	0.5	2.7	0.5	3.4
SnPO-2.00	68.3	55.5	81.3	2.1	0.3	8.6	0.8	6.9
SnPO-1.75[a]	99.7	93.0	93.3	1.6	0.4	1.2	0.4	3.1

[a] After a reaction time of 18 h.
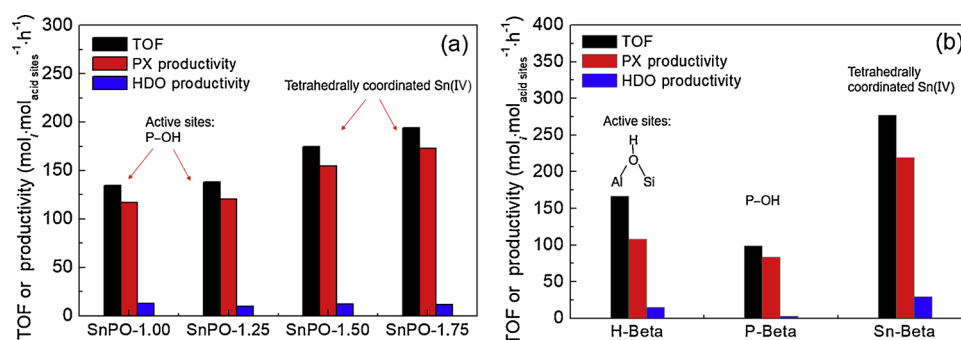
Fig. 5. TOF and productivity of PX and HDO over each catalyst in the reaction of DMF and ethylene to produce PX with a DMF conversion < 10%. (Reaction condition: DMF concentration, 1.04 M; acid site concentration, 0.8 mM; initial ethylene pressure, 2.0 MPa; reaction temperature, 250 °C; reaction duration: 0.5 h).

$\cdot\mathrm{mol_{acid\ sites}}^{-1\,h^{-1}}$ and 12 $\mathrm{mol_{HDO\ and\ MCP}}\cdot\mathrm{mol_{acid\ sites}}^{-1\,h^{-1}}$, respectively for the hydrolysis-derived products (HDO and MCP) than that of H-Beta (29 $\mathrm{mol_{HDO\ and\ MCP}}\cdot\mathrm{mol_{acid\ sites}}^{-1\,h^{-1}}$). Notably, MCP was only produced on H-Beta at low conversion (< 10%), suggesting that H-Beta had the strongest tendency to further converse HDO into intramolecularly or intermolecularly condensates. Although Sn-Beta exhibited the highest PX productivity of 219 $\mathrm{mol_{PX}}\cdot\mathrm{mol_{acid\ sites}}^{-1\,h^{-1}}$, the highest HDO productivity of 30 $\mathrm{mol_{HDO}}\cdot\mathrm{mol_{acid\ sites}}^{-1\,h^{-1}}$ was observed, making Sn-Beta have a lower selectivity for PX than SnPO-1.50 and SnPO-1.75.

Since hydrolysis and subsequent condensation are the main side reactions during PX production from DMF, a separate reaction of DMF and water to produce HDO was conducted in order to further investigate the catalytic activity of SnPO catalysts for them. Equal molar amount of $\mathrm{H_2O}$ and DMF were added into the reaction system without ethylene introduced. The TOF, the productivity of HDO and MCP, and carbon balance were shown in Fig. 6. The TOF value in the reaction of DMF and water to produce HDO was significantly lower than that in the reaction of DMF and ethylene to produce PX, revealing that PX production rather than DMF hydrolysis was more favored even at the presence of plenty of water. Sn-Beta and P-Beta showed significantly higher activity for the conversion of DMF (with TOF value of 128 $\mathrm{mol_{DMF}}\cdot\mathrm{mol_{acid\ sites}}^{-1\,h^{-1}}$ and 96 $\mathrm{mol_{DMF}}\cdot\mathrm{mol_{acid\ sites}}^{-1\,h^{-1}}$, respectively) and higher HDO productivity than other catalysts. Furthermore, a low carbon balance (42% and 48%, respectively) was observed on Sn-Beta and P-Beta, indicating they were also active for the condensation reactions, leading to a severe carbon loss. Although similar TOF values were obtained over SnPO-1.50, SnPO-1.75 and H-Beta, the SnPO catalysts exhibited a higher carbon balance in comparison with H-Beta, suggesting their lower activity for condensation reactions and better stability via inhibiting carbon deposition. Fig. S13 showed the product selectivity and carbon balance after a reaction duration of 6 h. A higher HDO selectivity accompanied by a lower selectivity for unknown products (mainly the condensation products of HDO) were observed on

SnPO catalysts than zeolite-based catalysts, confirming the lower activity of SnPO catalysts for the condensation reactions. Therefore, SnPO catalysts could achieve a higher carbon balance than zeolite-based catalysts.

Taken together the catalytic activity of SnPO and zeolite-based catalysts in the reaction of DMF and ethylene to form PX and the hydrolysis of DMF to form water, it could be concluded that tetrahedrally coordinated Sn(IV) was more effective for PX production. The outstanding PX selectivity over SnPO-1.50 and SnPO-1.75 mainly possessing tetrahedrally coordinated Sn(IV) as the active sites was attributed to the high productivity of PX and low productivity of HDO and sequent condensation products. Moreover, the low activity for the main side reaction, namely DMF hydrolysis and subsequent condensation further guaranteed the high stability of SnPO catalysts.

The reaction regime on SnPO-1.50 and H-Beta was investigated to compare the difference in activation energy. Experiments to investigate the reaction regime relative to acid site concentration were conducted on SnPO-1.50 and H-Beta at 250 °C and 200 °C by varying the catalyst loading. Fig. 7 shows the PX production rate versus the concentration of acid sites at the reaction of 0.5 h on SnPO-1.50 and H-Beta. The PX production rate appeared to be dependent on the concentration of acid sites. With the increased concentration of acid sites, the PX production rate first increased linearly and then reached a plateau when the concentration of acid sites was above 5.7 mM. That was because the overall rate was limited by the dehydration of the cycloadduct due to insufficient catalytic acid sites at low acid site concentration. At high concentration of acid sites, the overall rate was limited by the Diels-Alder reaction of DMF and ethylene which could be catalyzed by Lewis acid as reported by Caratzoulas, et al [15,47]. Furthermore, SnPO-1.50 exhibited a stronger PX production capacity than H-Beta under the identical acid sites concentration. The maximum PX production rate of SnPO-1.50 reached up to 10.9 mmol/h, which was 1.5 times higher than H-Beta (7.1 mmol/h). The product concentration and selectivity ralative to the acid site concentration on SnPO-1.50 were shown in Fig.
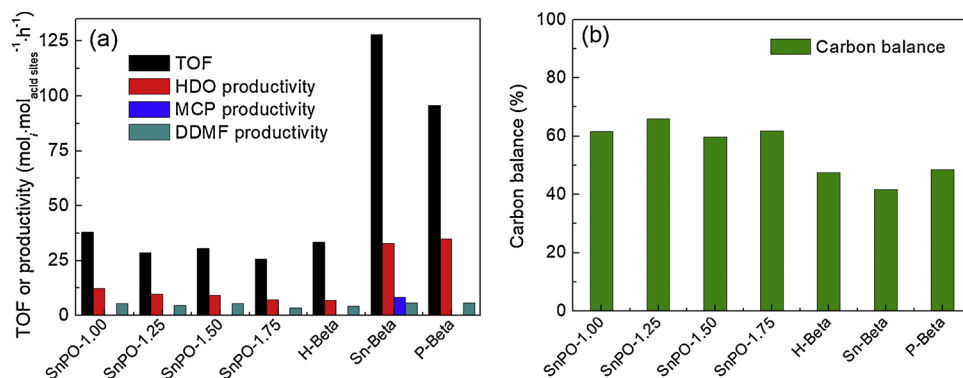
Fig. 6. TOF and productivity of product over each catalyst in the reaction of DMF and water to produce HDO and sequent condensation of HDO with a DMF conversion < 10%. (Reaction condition: DMF concentration, 1.04 M; acid site concentration, 0.8 mM; initial nitrogen pressure, 2.0 MPa; reaction temperature, 250 °C; reaction duration: 1 h).

DDMF represented the by-product dimer of DMF, derived from the oligomerization of DMF.

S14. With the increased concentration of acid sites, PX selectivity kept decreasing accompanied by an increasing HDO selectivity. High acid site concentration might accelerate the hydrolysis of DMF and cause the increased HDO selectivity.

The activation energies were measured on SnPO-1.50 and H-Beta by varying the reaction temperature in the range of 200–250 °C. The reaction of DMF and ethylene to form PX could be described by pseudo-first-order kinetics as reported [16,48]. At low acid site concentration (0.8 mM), the overall rate was limited by the dehydration of the cycloadduct, suggesting the activation energy corresponded to the dehydration reaction. The sum production rate of PX and OAP (derived from the further conversion of PX) at different reaction temperature was calculated according to Fig. S15 and Arrhenius plots of SnPO-1.50 and H-Beta at 0.8 mM acid site concentration were shown in Fig. 8(a). The linear least squares fit revealed activation energy of 14.6 kcal/mol for SnPO-1.50, which was slightly higher than H-Beta (13.0 kcal/mol). It was in accordance with the report that Brønsted acid exhibited a lower activation energy than Lewis acid [15]. While, SnPO-1.50 exhibited a higher PX production rate than H-Beta when the reaction temperature was above 200 °C, indicating a higher PX productivity in the actual operation temperature.

At high acid site concentration (5.7 mM), the overall rate was limited by the Diels-Alder reaction of DMF and ethylene to form cycloadduct which could be catalyzed by Lewis acid. The sum production rate of DA products (PX, DMCHO, and OAP) at different reaction temperature was calculated according to Fig. S16 and Arrhenius plots of SnPO-1.50 and H-Beta at 5.7 mM acid site concentration were shown in Fig. 8(b). The linear least squares fit revealed an activation energy of 19.5 kcal/mol for SnPO-1.50, which was lower than H-Beta (20.6 kcal/mol). SnPO-1.50 mainly possessing Lewis acid catalyzed the Diels-Alder reaction of DMF and ethylene. While, H-Beta, which was thought to be a Brønsted acid catalyst, exhibited no catalytic ability for the Diels-Alder reaction of DMF and ethylene as reported in the literature [15,17]. The lower activation energy of Diels-Alder reaction over SnPO-1.50 might lead to a higher

cycloadduct production rate, thus leading to a higher PX production rate than H-Beta when the reaction temperature was above 200 °C. That suggested that the existence of Lewis acid in SnPO-1.50 made it more active and productive for PX production than H-Beta. In addition, Eyring-Polanyi plots were used to calculate the activation entropy ($\Delta S^{\neq}$), activation enthalpy ($\Delta H^{\neq}$), and activation Gibbs energy ($\Delta G^{\neq}$) in the dehydration limited step and cycloaddition limited step, respectively as shown in Fig. S17 and Table S6. A smaller $\Delta G^{\neq}$ value for cycloaddition than dehydration was observed on both SnPO-1.50 and H-Beta, revealing a higher reaction rate constant for cycloaddition than dehydration under identical temperature according to the Equations S(1).

In addition, it was found that the selectivity for products was affected by both the acid site concentration and the reaction temperature as shown in Fig. S18 and Fig. S19. Higher PX selectivity was achieved at lower acid site concentration of 0.8 mM than higher acid site concentration of 5.7 mM because of the increased selectivity for HDO in the Diels–Alder cycloaddition limited regime. Sufficient acid sites accelerated the formation of HDO and MCP. In addition, the PX selectivity increased with the increase of reaction temperature accompanied by the decreased HDO selectivity. Fig. S20 shows the ratio of the production rate, in which the PX production rate is relative to the total production rate of PX and HDO as a function of the temperature. An increase in temperature promoted the formation of PX more efficiently than HDO, leading to an increased PX selectivity. The change in selectivity for MCP kept the same trend as HDO and the selectivity for OAP decreased with the increased reaction temperature. DMCHO, derived from the isomerization of cycloadduct, tended to have a higher selectivity at higher reaction temperature.

The influence of DMF concentration on the product selectivity was also been investigated. As shown in Fig. S21, PX selectivity decreased from 90.7% to 71.0% when the DMF concentration increased from 0.1 to 2.0 M. Higher DMF concentration was apt to produce more water and the produced water accelerated the hydrolysis of DMF as observed in Fig. S21 (HDO selectivity increased with increasing DMF
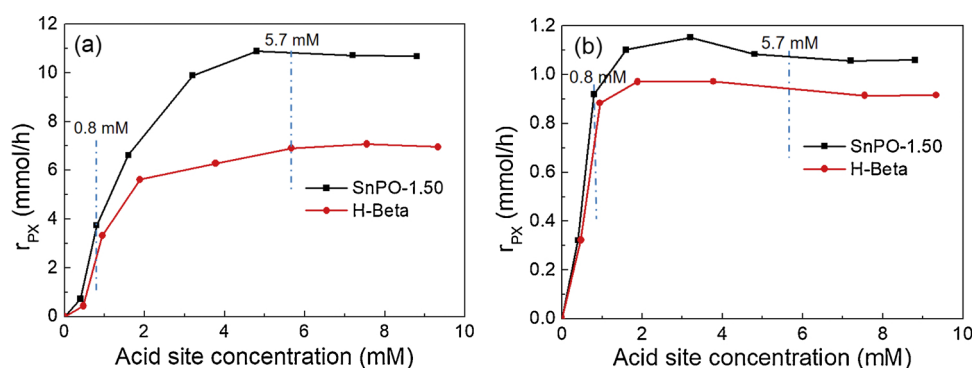
Fig. 7. PX production rate versus the concentration of acid sites on SnPO-1.50 and H-Beta at (a) 250 °C and (b) 200 °C. (Reaction condition: DMF concentration, 1.04 M; initial ethylene pressure, 2.0 MPa; reaction duration: 0.5 h).
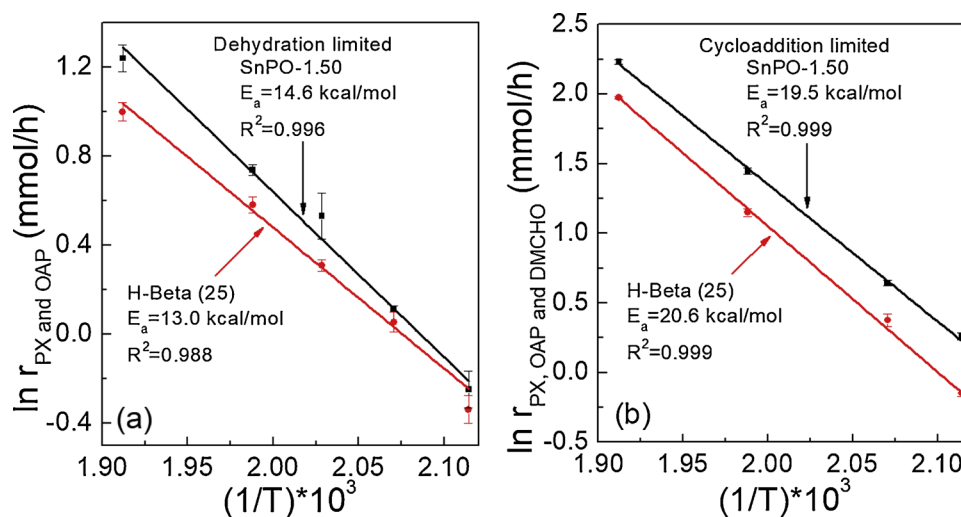
Fig. 8. (a) Arrhenius plot at 0.8 mM acid site concentration and (b) Arrhenius plot at 5.7 mM acid site concentration.

concentration). Considering the usage amount of the solvent and the selectivity for PX, DMF concentration of 1.0–1.5 M was generally used as reported in the literatures [17,21,24].

3.3. DFT calculation results

DFT calculations were carried out to provide deeper molecular insights into the role of the active sites on SnPO catalysts in the catalytic activity. Tetrahedrally coordinated Sn(IV) and PO−H were the active sites on the surface of SnPO catalysts and the models of the active sites for DFT calculations were shown in Fig. S22. As shown in Table S7, DMF was more easily absorbed on tetrahedrally coordinated Sn(IV) or PO−H active sites than ethylene. It was consistent with the TPD-MS experiments (Fig. S23). The desorption peak appeared at 128 °C and 62 °C when SnPO-1.50 adsorbed DMF or ethylene independently. However, when SnPO-1.50 adsorbed DMF and ethylene simultaneously, both the desorption peaks of DMF and ethylene appeared at 128 °C, indicating that DMF was interacting with the active sites and ethylene was absorbed on DMF. Therefore, the reaction started following the Eley-Rideal mechanism.

The mechanism for the formation of PX from DMF and ethylene was shown in Fig. 9(a) and the energy barriers were presented in Fig. 9(b). Tetrahedrally coordinated Sn(IV) or P−OH active sites combined the O atom of DMF and DMF underwent Diels-Alder reaction with ethylene to form the cycoladduct. The energy barriers revealed that tetrahedrally coordinated Sn(IV) active site could lower the energy barrier of uncatylzed 32.3 kcal/mol to 27.7 kcal/mol, while P−OH exhibited no catalytic activity. It was consistent with the report that Lewis acid could catalyze the Diels-Alder reaction of DMF and ethylene, while Brønsted acid could not [15,17]. The following dehydration could be divided into three steps: C−O cleavage, 1st proton transfer and 2nd proton transfer. The C−O cleavage required the highest energy barrier of 44.2 kcal/mol in the three steps. Tetrahedrally coordinated Sn(IV) active site exhibited a remarkably lower energy barrier (4.6 kcal/mol) of C−O cleavage than P−OH (30.4 kcal/mol), suggesting that tetrahedrally coordinated Sn(IV) was outstandingly more active for initiating dehydration reaction than P−OH. For the procedure of 1st proton transfer, tetrahedrally coordinated Sn(IV) active site and P−OH did not exhibit significant difference in the energy barrier. For the procedure of 2nd proton transfer, both tetrahedrally coordinated Sn(IV) active site and P−OH were very effective in reducing the energy barrier.

Thus, it could be concluded that tetrahedrally coordinated Sn(IV) active site was more effective in catalyzing the Diels-Alder cycloaddition reaction and the cleavage of C−O than P−OH. Therefore, SnPO-1.50 and SnPO-1.75 (tetrahedrally coordinated Sn(IV) as the active site)

exhibited higher PX selectivity and significantly higher PX productivity than SnPO-1.00 and SnPO-1.25 (P−OH as the active site).

3.4. Stability performance

The coke amount of spent catalyst after the reaction was analyzed by thermal gravimetry (TG) and the results were shown in Fig. S24 and Table S8. SnPO catalysts exhibited the less coke amount than all the zeolite-based zeolites. The spent catalysts H-Beta and SnPO-1.75 were characterized by ^{13}C CP-MAS NMR and FTIR to determine the composition of the coke. As shown in Figure S25, the presence of C = C, C = . S25, the presence of C=C, C=O, and aliphatic CH, CH$_2$, and CH$_3$ groups indicated that the coke was mainly derived from the condensation of HDO as suggested by Do, et al [9]. The composition of the coke was also investigated by FTIR as shown in Fig. S26. Several absorption peaks which were related to organic functional groups of the coke could be detected on the spent catalysts. The observed peaks were assigned to: 1460 cm^{-1}, the skeleton vibration in CH, CH$_2$, or CH$_3$ in aliphatic groups; 1640 cm^{-1}, the stretching vibrations of C=C; 1700 cm^{-1}, the stretching vibrations of carbonyl groups; 2870, 2930, and 2960 cm^{-1}, the stretching vibrations of CH, CH$_2$, and CH$_3$, respectively [49–51]. That verified again that the coke was mainly derived from the condensation of HDO. Therefore, the condensation of HDO formed the coke. Furthermore, the SnPO catalyst exhibited less coke (Table S8 and Fig. S25), indicating the weaker activity for hydrolysis and subsequent condensation reaction of HDO to form the coke than H-Beta.

The regeneration performances of SnPO-1.75 were tested in ten consecutive cyclic runs (reaction time of 6 h for each run) as shown in Fig. 10. In the first to fifth loop, the spent catalysts were regenerated by washing with ethanol. There was a continuous loss of activity because of the increased amount of carbon deposition covering the active sites. While, H-Beta was almost inactive after five recycles (Fig. S27), suggesting the importance of mesopores to resist catalyst coking. Therefore, SnPO-1.75 owned higher mass transfer efficiency and higher tolerance to deactivation caused by carbon deposition than H-Beta. Upon high-temperature calcination (550 °C, 6 h), the activity of SnPO-1.75 was fully recovered, confirming that SnPO-1.75 catalyst could be reused without activity losses in 10 consecutive runs. ICP results indicated a slight leaching of P (3%) from the bulk catalyst after ten consecutive cyclic runs. However, no obvious structure changes were observed on the regenerated catalyst proved by the XRD pattern and the SEM image of regenerated SnPO-1.75 as shown in Fig. S28(a) and (b), respectively.

The selectivity and stability of other reported catalysts were summarized in Table S9. For some supported acid catalysts such as SiO$_2$-
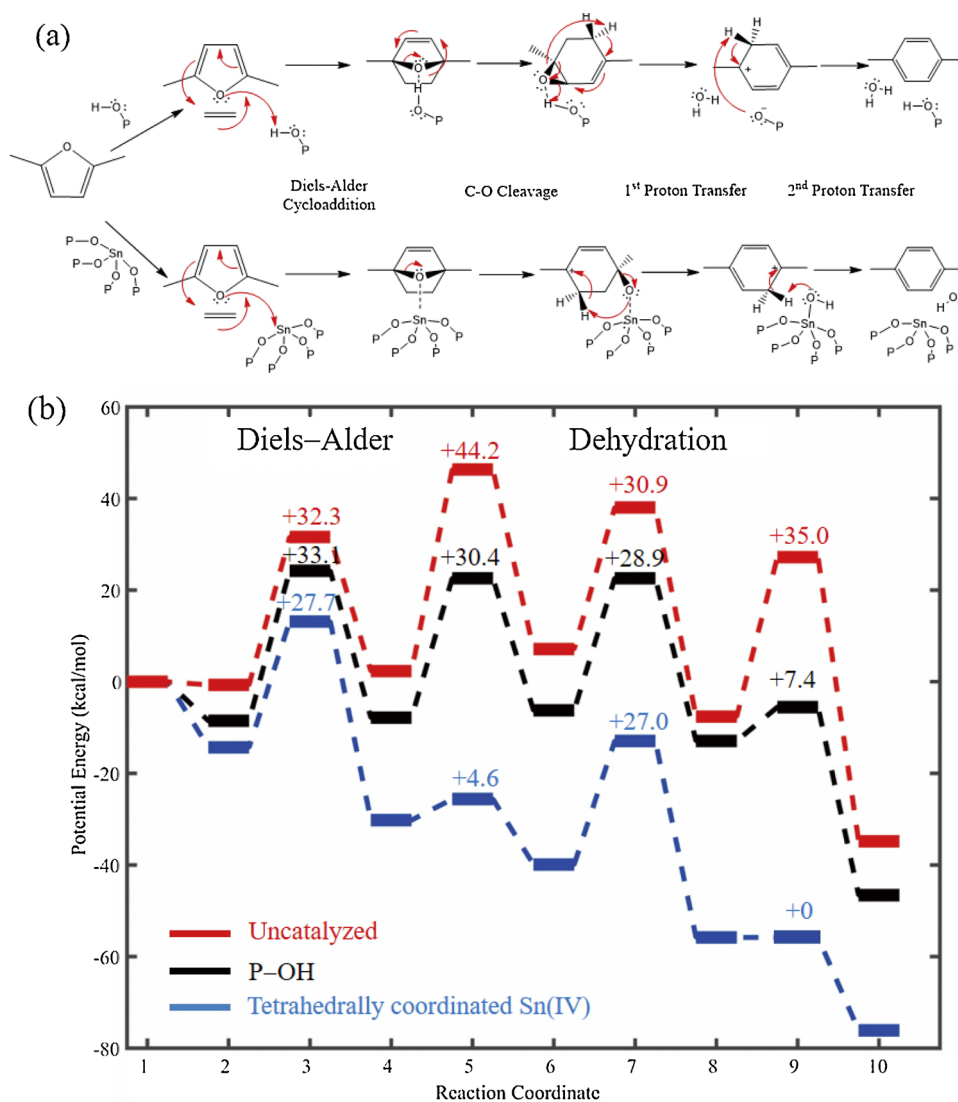
Fig. 9. (a) The mechanism and (b) the energy barriers for the formation of PX from DMF and ethylene.
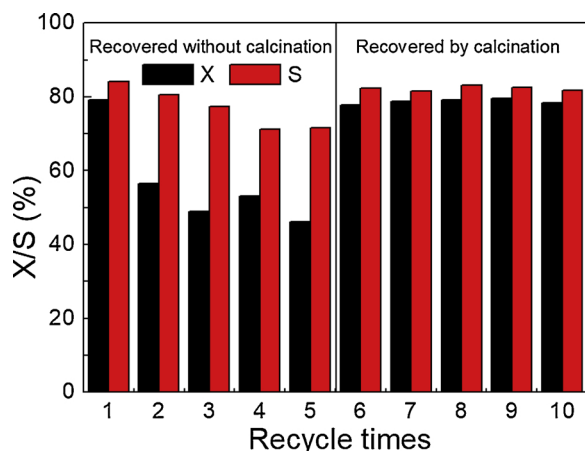

Fig. 10. Regeneration performances of SnPO-1.50 in 10 consecutive cyclic runs (Reaction condition: DMF concentration, 1.04 M; acid site concentration, 3.0 mM; initial ethylene pressure, 2.0 MPa; reaction temperature, 250 °C; reaction duration: 6 h).

SO$_3$H and P-BEA, although high selectivity (85% and 97%, respectively) was achieved, active sites might leach from the bulk material, leading to a poor reusability. SnPO-1.75 with a high stability was proved to be one of the most highly selective catalysts for the renewable PX production.

4. Conclusion

In this work, we developed SnPO as a highly promising catalyst for the production of renewable PX from the reaction of DMF and ethylene. By adjusting the molar ratio of P/Sn from 1.00 to 2.00 in the preparation course, the resulting SnPO exhibited different compositions of P/Sn, various surface structures and tunable Lewis and Brønsted acid properties. With the increase of the molar ratio of P/Sn in the material, the superstructure of SnPO changed from a disorderly accumulated structure to a planar layered structure and the main acid types changed from Brønsted acid to Lewis acid. SnPO-1.50 and SnPO-1.75 exhibited higher PX selectivity and significantly higher PX productivity than SnPO-1.00 and SnPO-1.25. It was concluded that tetrahedrally coordinated Sn(IV) in SnPO catalysts was more selective and efficient than P−OH groups for PX production. DFT calculations revealed that tetrahedrally coordinated Sn(IV) active site was more effective in catalyzing the Diels-Alder cycloaddition reaction and the cleavage of C−O than P−OH. In addition, their catalytic performances were compared with zeolite-based catalysts (H-Beta, Sn-Beta, and P-Beta) by kinetic studies. SnPO-1.75 exhibited a PX productivity of 173 mol$_{PX}$·mol$_{acid sites}^{-1}$ h^{-1}, which were nearly 1.5 times higher than that of H-Beta (108

$mol_{PX} \cdot mol_{acid\ sites}^{-1\,h^{-1}}$). In the meanwhile, it also demonstrated much lower activity for the hydrolysis side-reaction, giving a lower productivity of 12 $mol_{HDO\ and\ MCP} \cdot mol_{acid\ sites}^{-1\,h^{-1}}$ for the hydrolysis-derived products than that of H-Beta (29 $mol_{HDO\ and\ MCP} \cdot mol_{acid\ sites}^{-1\,h^{-1}}$). Besides, the SnPO catalyst manifested the least coke amount, outperforming H-Beta, Sn-Beta, and P-Beta. Furthermore, SnPO was proved to be stable and reusable, thus providing an alternative for the renewable PX production.

Declaration of Competing Interest

The authors declare no competing financial interest and conflicts.

Acknowledgements

Appendix A. Supplementary data

Supplementary material related to this article can be found, in the online version, at doi:https://doi.org/10.1016/j.apcatb.2019.118108.

References

[1] B. Xiao, M. Zheng, J. Pang, Y. Jiang, H. Wang, R. Sun, A. Wang, X. Wang, T. Zhang, Synthesis and characterization of poly(ethylene terephthalate) from biomass-based ethylene glycol: effects of miscellaneous diols, Ind. Eng. Chem. Res. 54 (2015) 5862–5869.

[2] R.A. Sheldon, Green and sustainable manufacture of chemicals from biomass: state of the art, Green Chem. 16 (2014) 950–963.

[3] M.-H. Qu, Y.-Z. Wang, C. Wang, X.-G. Ge, D.-Y. Wang, Q. Zhou, A novel method for preparing poly(ethylene terephthalate)/BaSO$_4$ nanocomposites, Eur. Polym. J. 41 (2005) 2569–2574.

[4] Z. Lin, M. Ierapetritou, V. Nikolakis, Aromatics from lignocellulosic biomass: economic analysis of the production of p-xylene from 5-hydroxymethylfurfural, AIChE J. 59 (2013) 2079–2087.

[5] J. Pang, M. Zheng, R. Sun, A. Wang, X. Wang, T. Zhang, Synthesis of ethylene glycol and terephthalic acid from biomass for producing PET, Green Chem. 18 (2016) 342–359.

[6] J.J. Pacheco, J.A. Labinger, A.L. Sessions, M.E. Davis, Route to renewable PET: reaction pathways and energetics of diels-alder and dehydrative aromatization reactions between ethylene and biomass-derived furans catalyzed by lewis acid molecular sieves, ACS Catal. 5 (2015) 5904–5913.

[7] P.C.A. Bruijnincx, B.M. Weckhuysen, Shale gas revolution: an opportunity for the production of biobased chemicals? Angew. Chemie Int. Ed. 52 (2013) 11980–11987.

[8] Z. Lin, V. Nikolakis, M. Ierapetritou, Alternative approaches for p-Xylene production from starch: techno-economic analysis, Ind. Eng. Chem. Res. 53 (2014) 10688–10699.

[9] P.T.M. Do, J.R. McAtee, D.A. Watson, R.F. Lobo, Elucidation of diels–Alder reaction network of 2,5-Dimethylfuran and ethylene on HY zeolite catalyst, ACS Catal. 3 (2013) 41–46.

[10] C.-C. Chang, S.K. Green, C.L. Williams, P.J. Dauenhauer, W. Fan, Ultra-selective cycloaddition of dimethylfuran for renewable p-xylene with H-BEA, Green Chem. 16 (2014) 585–588.

[11] K.S. Arias, M.J. Climent, A. Corma, S. Iborra, Synthesis of high quality alkyl naphthenic kerosene by reacting an oil refinery with a biomass refinery stream, Energy Environ. Sci. 8 (2015) 317–331.

[12] G.H. Wang, J. Hilgert, F.H. Richter, F. Wang, H.J. Bongard, B. Spliethoff, C. Weidenthaler, F. Schüth, Platinum-cobalt bimetallic nanoparticles in hollow carbon nanospheres for hydrogenolysis of 5-hydroxymethylfurfural, Nat. Mater. 13 (2014) 293–300.

[13] B. Chen, F. Li, Z. Huang, G. Yuan, Carbon-coated Cu-Co bimetallic nanoparticles as selective and recyclable catalysts for production of biofuel 2,5-dimethylfuran, Appl. Catal. B Environ. 200 (2017) 192–199.

[14] W. Guo, H.H. Liu, S. Zhang, H. Han, H.H. Liu, T. Jiang, B. Han, T. Wu, Efficient hydrogenolysis of 5-hydroxymethylfurfural to 2,5-dimethylfuran over a cobalt and copper bimetallic catalyst on N-graphene-modified Al$_2$O$_3$, Green Chem. 18 (2016) 6222–6228.

[15] N. Nikbin, P.T. Do, S. Caratzoulas, R.F. Lobo, P.J. Dauenhauer, D.G. Vlachos, A DFT study of the acid-catalyzed conversion of 2,5-dimethylfuran and ethylene to p-xylene, J. Catal. 297 (2013) 35–43.

[16] J. Yu, S. Zhu, P.J. Dauenhauer, H.J. Cho, W. Fan, R.J. Gorte, Adsorption and reaction properties of SnBEA, ZrBEA and H-BEA for the formation of p-xylene from

[17] C.-C. Chang, H. Je Cho, J. Yu, R.J. Gorte, J. Gulbinski, P. Dauenhauer, W. Fan, Lewis acid zeolites for tandem Diels–Alder cycloaddition and dehydration of bio-mass-derived dimethylfuran and ethylene to renewable p-xylene, Green Chem. 18 (2016) 1368–1376.

[18] L. Tao, T.H. Yan, W. Li, Y. Zhao, Q. Zhang, Y.M. Liu, M.M. Wright, Z.H. Li, H.Y. He, Y. Cao, Toward an integrated conversion of 5-Hydroxymethylfurfural and ethylene for the production of renewable p-Xylene, Chem. 4 (2018) 2212–2227.

[19] C.L. Williams, C.-C.C. Chang, P. Do, N. Nikbin, S. Caratzoulas, D.G. Vlachos, R.F. Lobo, W. Fan, P.J. Dauenhauer, Cycloaddition of biomass-derived furans for catalytic production of renewable p-xylene, ACS Catal. 2 (2012) 935–939.

[20] J.-C.C. Kim, T.-W.W. Kim, Y. Kim, R. Ryoo, S.-Y.Y. Jeong, C.-U.U. Kim, Mesoporous MFI zeolites as high performance catalysts for Diels-Alder cycloaddition of bio-derived dimethylfuran and ethylene to renewable p-xylene, Appl. Catal. B Environ. 206 (2017) 490–500.

[21] H.J. Cho, L. Ren, V. Vattipalli, Y.-H. Yeh, N. Gould, B. Xu, R.J. Gorte, R. Lobo, P.J. Dauenhauer, M. Tsapatsis, W. Fan, Renewable p-Xylene from 2,5-Dimethylfuran and ethylene using phosphorus-containing zeolite catalysts, ChemCatChem. 9 (2017) 398–402.

[22] R. Zhao, Z. Zhao, S. Li, A.N. Parvulescu, U. Müller, W. Zhang, Excellent performances of dealuminated H-Beta zeolites from organotemplate-free synthesis in conversion of biomass-derived 2,5-Dimethylfuran to renewable p-Xylene, ChemSusChem. 11 (2018) 3803–3811.

[23] T.-W.W. Kim, S.-Y.Y. Kim, J.-C.C. Kim, Y. Kim, R. Ryoo, C.-U.U. Kim, Selective p-xylene production from biomass-derived dimethylfuran and ethylene over zeolite beta nanosponge catalysts, Appl. Catal. B Environ. 185 (2016) 100–109.

[24] Y. Philip, H. Pandu, Y. Park, D. Jin, H. Lee, J. Ha, J. Jae, Heteropolyacid catalysts for Diels-Alder cycloaddition of 2,5-dimethylfuran and ethylene to renewable p-xylene, Catal. Today 293–294 (2017) 167–175.

[25] D. Wang, C.M. Osmundsen, E. Taarning, J.A. Dumesic, Selective production of aromatics from alkylfurans over solid acid catalysts, ChemCatChem. 5 (2013) 2044–2050.

[26] A. García, M. Colilla, I. Izquierdo-Barba, M. Vallet-Regí, Incorporation of phosphorus into mesostructured silicas: a novel approach to reduce the SiO$_2$ leaching in water, Chem. Mater. 21 (2009) 4135–4145.

[27] C. Serre, A. Auroux, A. Gervasini, M. Hervieu, G. Férey, Hexagonal and cubic thermally stable mesoporous tin(IV) phosphates with acidic and catalytic properties, Angew. Chemie - Int. Ed. 41 (2002) 1594–1597.

[28] K.T.V. Rao, S. Souzanchi, Z. Yuan, M.B. Ray, C. (Charles) Xu, Simple and green route for preparation of tin phosphate catalysts by solid-state grinding for dehydration of glucose to 5-hydroxymethylfurfural (HMF), RSC Adv. 7 (2017) 48501–48511.

[29] T. Okuhara†, T. Okuhara, Water-tolerant solid acid catalysts, Chem. Rev. 102 (2002) 3641–3666.

[30] X. Wang, F. Liang, C. Huang, Y. Li, B. Chen, Highly active tin(iv) phosphate phase transfer catalysts for the production of lactic acid from triose sugars, Catal. Sci. Technol. 5 (2015) 4410–4421.

[31] R. Weingarten, Y.T. Kim, G.A. Tompsett, A. Fernández, K.S. Han, E.W. Hagaman, W.C. Conner, J.A. Dumesic, G.W. Huber, Conversion of glucose into levulinic acid with solid metal(IV) phosphate catalysts, J. Catal. 304 (2013) 123–134.

[32] Q. Hou, M. Zhen, L. Liu, Y. Chen, F. Huang, S. Zhang, W. Li, M. Ju, Tin phosphate as a heterogeneous catalyst for efficient dehydration of glucose into 5-hydroxymethylfurfural in ionic liquid, Appl. Catal. B Environ. 224 (2018) 183–193.

[33] A. Dutta, D. Gupta, A.K. Patra, B. Saha, A. Bhaumik, Synthesis of 5-hydroxymethylfururual from carbohydrates using large-pore mesoporous tin phosphate, ChemSusChem. 7 (2014) 925–933.

[34] J.C. Vega-Vila, J.W. Harris, R. Gounder, Controlled insertion of tin atoms into zeolite framework vacancies and consequences for glucose isomerization catalysis, J. Catal. 344 (2016) 108–120.

[35] M.J. Frisch, G.W. Trucks, H.B. Schlegel, G.E. Scuseria, M.A. Robb, J.R. Cheeseman, G. Scalmani, V. Barone, B. Mennucci, G.A. Petersson, H. Nakatsuji, M. Caricato, X. Li, H.P. Hratchian, A.F. Izmaylov, J. Bloino, G. Zheng, J.L. Sonnenberg, M. Hada, M. Ehara, K. Toyota, R. Fukuda, J. Hasegawa, M. Ishida, T. Nakajima, Y. Honda, O. Kitao, H. Nakai, T. Vreven, J.A.J. Montgomery, J.E. Peralta, F. Ogliaro, M. Bearpark, J.J. Heyd, E. Brothers, K.N. Kudin, V.N. Staroverov, R. Kobayashi, J. Normand, K. Raghavachari, A. Rendell, J.C. Burant, S.S. Iyengar, J. Tomasi, M. Cossi, N. Rega, J.M. Millam, M. Klene, J.E. Knox, J.B. Cross, V. Bakken, C. Adamo, J. Jaramillo, R. Gomperts, R.E. Stratmann, O. Yazyev, A.J. Austin, R. Cammi, C. Pomelli, J.W. Ochterski, R.L. Martin, K. Morokuma, V.G. Zakrzewski, G.A. Voth, P. Salvador, J.J. Dannenberg, S. Dapprich, A.D. Daniels, O. Farkas, J.B. Foresman, J.V. Ortiz, J. Cioslowski, D.J. Fox, Gaussian 09 (Rev. A.2), Gaussian Inc., Wallingford, CT, 2009.

[36] M. Gu, D. Yu, H. Zhang, P. Sun, H. Huang, Metal(IV) phosphates as solid catalysts for selective dehydration of sorbitol to Isosorbide, Catal. Lett. 133 (2009) 214–220.

[37] J. Yin, C. Shen, X. Feng, K. Ji, L. Du, Highly selective production of p-xylene from 2,5-dimethylfuran over hierarchical NbOx-based catalyst, ACS Sustain. Chem. Eng. 6 (2018) 1891–1899.

[38] X. Feng, C. Shen, K. Ji, J. Yin, T. Tan, Production of p-xylene from bio-based 2,5-dimethylfuran over high performance catalyst WO$_3$/SBA-15, Catal. Sci. Technol. 7 (2017) 5540–5549.

[39] H. Qiao, F. Jia, Z. Ai, Z. Li, L. Zhang, One-pot synthesis of spring-like super-structures consisting of layered tin(iv) hydrogen phosphate nanodisks, Chem. Commun. 0 (2006) 2033–2035.

[40] M. Paul, N. Pal, B.S. Rana, A.K. Sinha, A. Bhaumik, New mesoporous titanium-phosphorus mixed oxides having bifunctional catalytic activity, Catal. Commun. 10 (2009) 2041–2045.

[41] V.V.V. Ordomsky, V.L.L. Sushkevich, J.C.C. Schouten, J. van der Schaaf, T.A.A. Nijhuis, Glucose dehydration to 5-hydroxymethylfurfural over phosphate catalysts, J. Catal. 300 (2013) 37–46.

[42] J. Dijkmans, M. Dusselier, D. Gabriëls, K. Houthoofd, P.C.M.M. Magusin, S. Huang, Y. Pontikes, M. Trekels, A. Vantomme, L. Giebeler, S. Oswald, B.F. Sels, Cooperative catalysis for multistep biomass conversion with Sn/Al Beta zeolite, ACS Catal. 5 (2015) 928–940.

[43] J. Dijkmans, D. Gabriëls, M. Dusselier, F. de Clippel, P. Vanelderen, K. Houthoofd, A. Malfliet, Y. Pontikes, B.F. Sels, Productive sugar isomerization with highly active Sn in dealuminated β zeolites, Green Chem. 15 (2013) 2777–2785.

[44] H. Li, J. He, A. Riisager, S. Saravanamurugan, B. Song, S. Yang, Acid–Base bi-functional zirconium N-Alkyltriphosphate nanohybrid for hydrogen transfer of biomass-derived carboxides, ACS Catal. 6 (2016) 7722–7727.

[45] H.J.M. Bosman, A.P. Pijpers, A.W.M.A. Jaspers, An X-Ray photoelectron spectro-scopy study of the acidity of SiO$_2$–ZrO$_2$ mixed oxides, J. Catal. 161 (1996) 551–559.

[46] X. Feng, C. Shen, C. Tian, T. Tan, Highly selective production of Biobased p-Xylene from 2,5-Dimethylfuran over SiO$_2$–SO$_3$H catalysts, Ind. Eng. Chem. Res. 56 (2017) 5852–5859.

[47] N. Nikbin, S. Feng, S. Caratzoulas, D.G. Vlachos, P-xylene formation by dehydrative aromatization of a Diels–Alder product in Lewis and brønsted acidic zeolites, J. Phys. Chem. C. 118 (2014) 24415–24424.

[48] C.L. Williams, K.P. Vinter, C.C. Chang, R. Xiong, S.K. Green, S.I. Sandler, D.G. Vlachos, W. Fan, P.J. Dauenhauer, Kinetic regimes in the tandem reactions of H-BEA catalyzed formation of p-xylene from dimethylfuran, Catal. Sci. Technol. 6 (2016) 178–187.

[49] Y.P. Wijaya, I. Kristianto, H. Lee, J. Jae, Production of renewable toluene from biomass-derived furans via Diels-Alder and dehydration reactions: a comparative study of Lewis acid catalysts, Fuel. 182 (2016) 588–596.

[50] E. Epelde, M. Ibañez, A.T. Aguayo, A.G. Gayubo, J. Bilbao, P. Castaño, Differences among the deactivation pathway of HZSM-5 zeolite and SAPO-34 in the transfor-mation of ethylene or 1-butene to propylene, Microporous Mesoporous Mater. 195 (2014) 284–293.

[51] H. Zhang, S. Shao, R. Xiao, D. Shen, J. Zeng, Characterization of coke deposition in the catalytic fast pyrolysis of biomass derivates, Energy Fuels 28 (2014) 52–57.